In Situ X-Ray tomography studies of microstructural evolution combined with 3D modelling

Jean-Yves Buffiere, Peter Cloetens, Wolfgang Ludwig, E. Maire, Luc Salvo

In Situ X-Ray Tomography Studies of Microstructural Evolution Combined with 3D Modeling

J.-Y. Buffière, P. Cloetens, W. Ludwig, E. Maire, and L. Salvo

Synchrotron x-ray microtomography is a characterization technique increasingly used to obtain 3D images of the interior of optically opaque materials with a spatial resolution in the micrometer range. As a nondestructive technique, it enables the monitoring of microstructural evolution during *in situ* experiments. In this article, examples from three different fields of metals research illustrate the contribution of x-ray tomography data to modeling: deformation of cellular materials, metal solidification, and fatigue crack growth in Al alloys. Conventionally, tomography probes the 3D distribution of the x-ray attenuation coefficient within a sample. However, this technique is also being extended to determine the local crystallographic orientation in the bulk of materials (diffraction contrast tomography), a key issue for the modeling of microstructure in metals.

Introduction

The development of functional or structural materials with improved performance, sometimes under extreme environmental conditions, requires a detailed knowledge of their microstructure and of the mechanisms controlling their behavior. Classical research in this field has extensively involved—and still involves—*post mortem* characterization of samples. Very often, however, *in situ* observation is more desirable, either because "standard" conditions of observation are not representative of operating conditions (room temperature versus high temperature, for example) or because the chronology of microstructural evolution is a key issue (e.g., nucleation of cavities formed under load versus growth and coalescence of such cavities).

At a macroscopic level (i.e., spatial resolution from 100 μm and above), well-established *in situ* experimental techniques provide global information on the evolution of material microstructures. For instance, acoustic and stiffness tests can measure the development of internal damage in a material during mechanical loading at various temperatures. The measurements are relevant for developing constitutive equations of the mechanical behavior of a structural material.

However, investigating the physical mechanisms that are responsible for such macroscopic evolution requires characterization at a much finer scale, typically in the micrometer range or below. Various types of microscopy, including optical and electron microscopy, provide valuable insights into microstructural evolution when used at the surface of samples, but the applicability of the findings to the bulk of the material remains questionable. In the field of damage development under load, for example, some studies have clearly shown discrepancies between results obtained in the bulk and at the surface of strained samples.[1,2] Therefore, there is a great need in materials science for characterization methods that provide images of the interior of samples, if possible, nondestructively and with a high spatial resolution; tomography is one of them.

Computed tomography consists of using software to reconstruct a quantity from the knowledge of its projections for a large number of angular orientations (integrals along lines). Although the main principle of tomography has been known since as early as 1917,[3] it was not put into practice until the early 1970s when it was used in medical applications at a macroscopic scale.[4,5] Since the 1990s, the spatial resolution has rapidly improved to the micrometer and submicrometer scale, thanks to the availability of powerful synchrotron x-ray sources.[6–9] Today, computed tomography is a major characterization method for materials science applications.[10] Currently, high-resolution x-ray tomography is the only nondestructive technique that provides three-dimensional (3D) images of the interior of arbitrary (metal, ceramic, polymer, composite, crystalline, amorphous) optically opaque materials on "reasonably large" (millimeter-sized) samples with a spatial resolution comparable to that of optical microscopy. Laboratory instruments have now also become available, either based on commercial turnkey systems[11] or as centralized user facilities.[12,13] Compared to synchrotron sources, laboratory sources are somewhat restricted for high-resolution *in situ* characterization. The signal-to-noise ratio, sensitivity, and scan duration are limited by the useful flux, which is orders of magnitude smaller than in the case of a synchrotron source. Fast tomography (scan duration on the order of one minute) is therefore not achievable on a laboratory source. Different approaches to improve the spatial resolution to the 50–100-nm range have been proposed and are under active development.[9,14,15] They rely on the use of x-ray optics to overcome the spatial resolution limitations imposed by the x-ray imaging detector.

Alongside characterization methods, modeling strategies in materials science have also evolved during the past 10 years toward a 3D approach. Ideally, the modeling of material behavior should be based on a realistic description of the microstructure and the underlying processes, which are often 3D in nature.

Depending on the problem being addressed, different methods have been used to obtain realistic digital 3D microstructures as input for models. Other articles in this issue present these methods. Automated serial sectioning has

been used, for example, to acquire information on the evolution of the interfacial shape during coarsening of two-phase alloys.[16] Three-dimensional arrangements of grains and their local crystallography have also been obtained by orthogonal electron backscatter diffraction (EBSD) maps and a voxel-based tessellation technique[17,18] or by serial sectioning coupled with EBSD;[19] in the latter case, serial sectioning is performed either by mechanical polishing or by focused ion beam (FIB) machining.[19] See the articles by Spanos et al. and Kammer et al. in this issue. Such 3D digital microstructures can be used for modeling the mechanical responses of polycrystalline aggregates.[20,21] Their obvious disadvantage is that they are obtained in a destructive manner. They generally provide an initial state for modeling, except when each microstructure is statistically characterized,[22] in which case information on the evolution can also be obtained.

High-resolution x-ray tomography is a powerful experimental tool that can complement these techniques by providing 3D images of microstructures nondestructively. We show some examples of the use of these images for finite element modeling and focus on *in situ* x-ray tomography experiments that supply not only the initial state of the material microstructure but also its evolution under various experimental conditions. The limits of the technique are also described, and possible developments that aim to overcome these limits are presented.

Tomography Setup

Several experimental stations (beamlines) at various synchrotron facilities all over the world offer the possibility of performing x-ray microtomography, including the Advanced Photo Source in the United States, Spring-8 in Japan, and the Swiss Light Source in Switzerland.[23–28] The European Synchrotron Radiation Facility (ESRF) in Grenoble, France, is a pioneering synchrotron source in this field of research. Currently, three beamlines routinely offer the possibility of performing x-ray tomography at the ESRF. Each beamline has distinct capabilities:[7] high x-ray energy and fast tomography, high throughput and phase-contrast tomography, and high spatial resolution and fluorescence tomography.

The permanent microtomographic setup at the high throughput beamline at ESRF (ID19) provides an example for describing an x-ray tomography layout. The beamline was designed to perform experiments giving 3D microstructural images with a voxel size ranging from 0.3 μm to several tens of microns each side depending on the detector used. (A voxel is the smallest elementary volume element composing 3D images. It is therefore the 3D equivalent of the pixel in classical two-dimensional images.) Obtaining a tomographic image first involves recording a series of N (~1,500) radiographs of a sample as it is rotated about one axis. Reconstruction software then implements a filtered backprojection algorithm on the N radiographs to create a 3D numerical image. The image is a 3D map of the attenuation coefficient in the sample.

The charge-coupled device (CCD) camera recording the radiographs on this beamline records at a rate of 40 megapixels/s or 110 ms/image on to a square array of 2,048 × 2,048 pixels. For a tomography experiment, the white beam emerging from the synchrotron ring is rendered monochromatic by a multilayer monochromator, and the energy of the beam can be tuned from 10 keV to around 60 keV. An exceptionally long source-to-specimen distance in a tomography setup, such as 145 m as found on beamline ID19, can provide a partially coherent x-ray beam introducing virtually no geometrical blur when the sample-to-detector distance is increased (less than 1 μm blur with a 1-m sample-to-detector distance). This design allows for two useful experimental features. First, it provides an easy setup for phase-contrast tomography based on free space propagation and the associated Fresnel diffraction.[33] A tomography scan acquired at finite (small) distance will then obtain, in addition to the degree of x-ray absorption, the degree of phase-contrast related to the changes in refractive index or electron density in the sample. This is a very efficient approach of enhancing the contrast of boundaries and cracks. Quantitative 3D reconstruction of the refractive index itself is possible by applying a phase-retrieval procedure before the tomographic reconstruction of the 2D radiographs, but this typically requires tomographic scans at a few different distances. The combined technique is called holotomography.[7]

The second feature accompanying the long source-to-specimen design is that the space available in front of the CCD detector enables *in situ* investigations under various types of experimental conditions. The space enables the installation of tailored experimental devices such as cold cells, furnaces, or mechanical testing devices. On high-resolution laboratory setups, this space is typically not available, as the sample needs to be very close to the x-ray source (divergent beam).

Mechanical Behavior of Cellular Materials

The cellular materials considered in this section are mixtures of solid and gaseous phases, that is, they contain a high amount (roughly >70%) of porosity. Their outstanding properties and the scientific challenges involved in modeling their properties are reviewed in the book by Gibson and Ashby.[34] In these materials, the architecture of the solid phase defines cells, where each cell consists of a single pore and the surrounding fraction of solid. The pores can be sealed (closed-cell foam), or they can form an interconnected network (open-cell foam). Nondestructive 3D imaging is a key issue in the case of cellular materials. It is very difficult to obtain a good description of the spatial distribution and arrangement between gas and solid with conventional microscopy methods, as deformation in these materials involves significant out-of-plane components, so their modeling and deformation should also be analyzed in three dimensions. The different articles from the literature cited in this section show that cellular materials can be well characterized using x-ray tomography. Images of representative volumes of materials at the relevant scale of the microstructure are thus available.

A vital question is how to represent the information from the tomography as input for finite element (FE) calculations[35,36,37] in order for the FE model to reproduce the microstructure as exactly as possible while still remaining amenable to computational simulation.

Three different strategies can be used to produce meshes picturing the 3D data sets, as summarized in Figure 1. The most straightforward technique consists of replacing each voxel of the 3D data set by a cubic element of the same size[38,39] (method 1 in Figure 1). A second technique (method 2 in Figure 1), developed for cellular materials[40] and more recently used for a bulk material,[41] consists of meshing the outer surface of each phase in the microstructure using triangular elements. The solid part of the microstructure defined by the outer surfaces is meshed in this method by an advanced front technique[40] using tetrahedral volume elements starting from a surface mesh. If the material is a cellular material (that is, contains a large amount of porosity), another method can be used provided that a graph (or skeleton) of the solid phase can be calculated. Instead of completely meshing the solid phase, it is sometimes sufficient for the structures of these materials to be simplified by means of beam[42,43] or shell elements (method 3 in Figure 1).

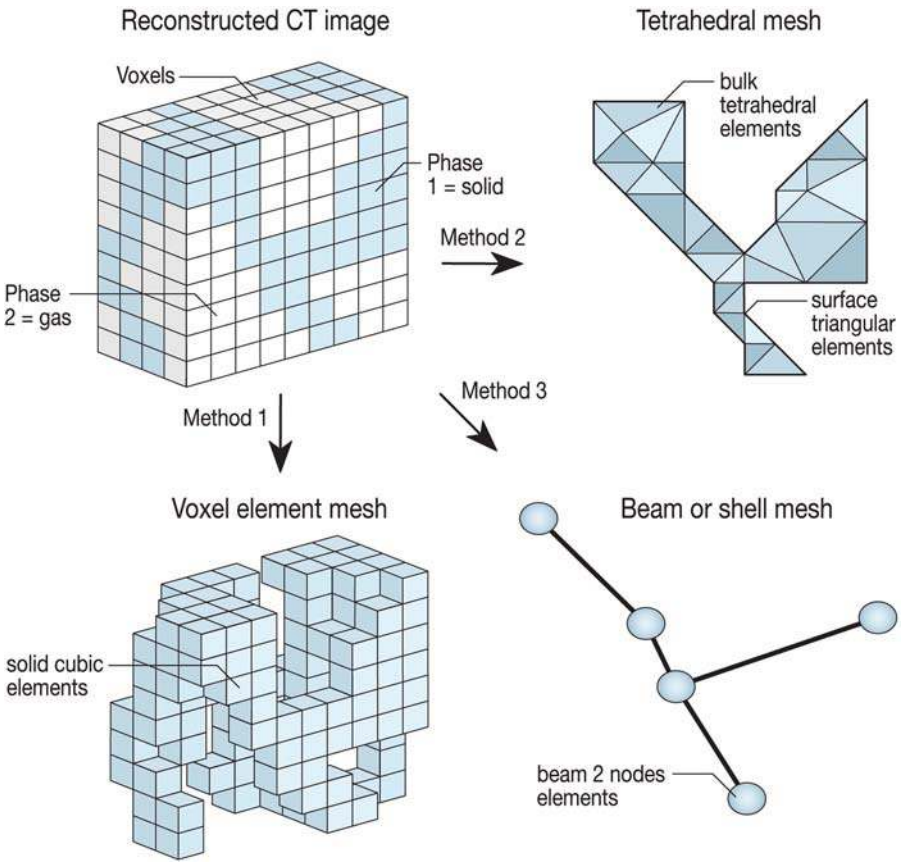

Figure 1. Schematic description of three methods for transforming a tomographic voxel reconstruction of a two-phase material into a finite element mesh. For the sake of simplicity, the description is presented in two dimensions.

The FE modeling of closed-cell foams cannot be carried out using beam elements. For these materials, method 1 or 2 could possibly be used.[40] An example of a comparison between an experimental test and such a calculation using method 2 is shown in Figure 2. Figures 2a and 2b show, respectively, the initial and deformed states of a metal hollow-sphere structure during a fatigue test performed in compression, and Figure 2c shows a contour plot of the local stresses calculated in compression for the total sample. The result of the calculations can be post-processed to determine the weak points of the microstructure under a given (arbitrary) load. For Figure 2c, a simple post-processing—calculation of the von Mises stress in each element—was performed. The calculation showed that this stress is higher in regions where the material deforms highly in the experimental observations. In the different studies where this local comparison has been achieved (see, for example, Reference 40), a clear relationship has always been found between stress concentration and local deformation.

Very low-density materials can contain walls that are extremely thin compared to the size of the cells.[44] However, a new method can be used to design a mesh that reproduces the microstructure of a real tomographic data set for the case of closed-cell cellular materials. The new method augments method 3 by using shell elements with a realistic thickness. The method is based on a skeletonization of the solid phase by thinning.[45] Each cell of the gaseous phase must first be labeled. Each label can then be dilated isotropically through the solid phase until it encounters the neighboring concurrently dilating gaseous phase. At the end of this dilation procedure, the solid phase has been eliminated, and the interface between two neighboring cells lies exactly in the middle of the previously existing wall between these two cells. This interface can be meshed using surface (shell) triangular elements and can then be simplified to reduce the number of triangles while preserving a good description of the surface. It is then possible to measure locally the actual thickness of the wall in the tomographic image and to assign this more realistic thickness to the corresponding finite shell element. Such a realistic mesh could, for instance, be used to compute the global behavior of many cellular materials. Furthermore, it could also be used to simulate the behavior under more complex stress states such as multiaxial loading, which, in some cases, is difficult to obtain experimentally.

Semisolid Microstructures

The characterization of materials in the semisolid state (either during isothermal heat treatment or during solidification) is not easy to perform. An important feature is the spatial resolution required. There are generally two scales in the microstructure: that of the solid phase (typical dimensions on the order of 100–200 μm) and that of the liquid films (typical dimensions of ~5–0.5 μm). As the connectivity of solid/liquid phases cannot be assessed on 2D images, the ability to obtain 3D images is a crucial issue for semisolid microstructures. Two main techniques have been used for 3D characterization of semisolid structures: serial sectioning,[46–53] which will not be presented here but is covered in accompanying articles by Kammer et al. and Spanos et al., and x-ray tomography, described next.

X-Ray Microtomography on Quenched Samples

X-ray microtomography has been successfully used to characterize semisolid structures in quenched conditions on various alloys including Al–Cu and Al–Ge in conventional absorption mode[54,55] and Al–Mg–Si and AZ91 in phase-contrast[56,57] or holotomography[7] mode. Interrupted tomography experiments were performed on the same sample to study the microstructural evolution in the semisolid state in Al–Si and Al–Cu alloys.[56] However, performing x-ray tomography on quenched samples can induce errors in parameter estimation such as solid particle size or solid–liquid interfacial area; to avoid this problem, it has been shown that the quench rate must be on the order of 100°C/s,[58] which is difficult to obtain in practice.

In Situ Characterization

The difficulties associated with quenching samples of semisolid materials can be avoided by performing measurements *in situ.* Three-dimensional *in situ* characterization with a spatial resolution on the order of a few microns is now possible thanks to ultrafast x-ray tomography, which operates according to the principles of conventional x-ray tomography but

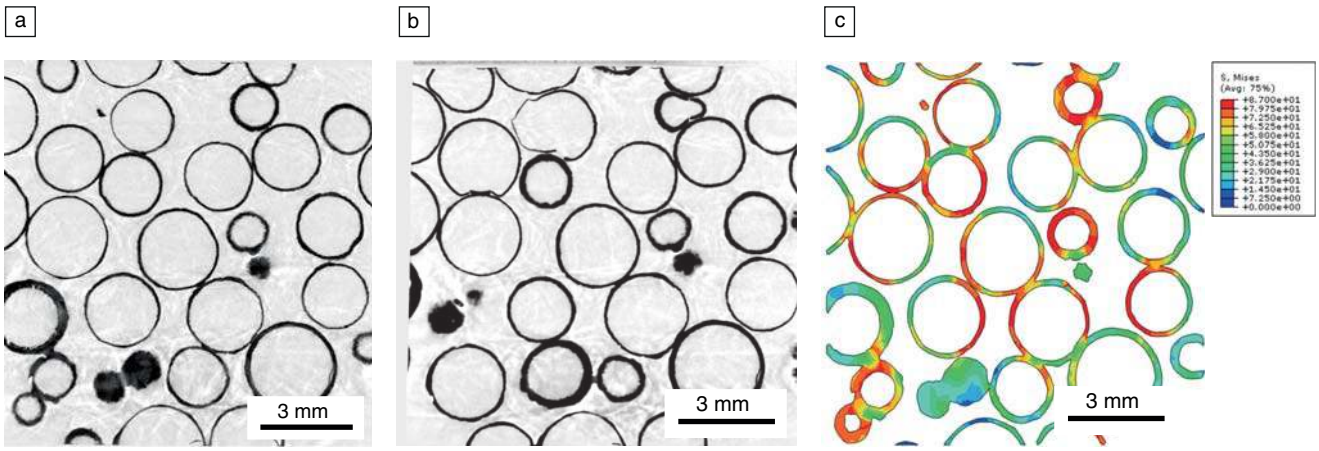

Figure 2. (a, b) Two-dimensional tomographic slices extracted from the reconstructions of the same sample at two different stages of the fatigue life during a compression *ex situ* fatigue test: (a) initial state, (b) after fatigue deformation. The sample was made of sintered hollow 316L spheres. (c) Contour plot of the value of the von Mises stress calculated in the same slice as in part a using method 2. The size of the tomogram was 719 × 681 × 642 voxels, the mesh contained 133,824 nodes and 428,391 elements, and the calculation was carried out in 8,166 CPU seconds (Intel Xeon processor, 3.2 GHz CPU, 2 GB RAM). High-stress areas (in red) appear to be concomitant with some deformation sites in Figure 2b. Adapted from Reference 90.

invloves experiments that are performed using faster cameras and a continuous acquisition mode.[59] To reduce the total scan time, the number of projections, the exposure time, and the spatial resolution are optimized.[60] As already mentioned, ultrafast tomography requires a high x-ray flux and thus is only possible using synchrotron sources. In practice, the duration, D, of a complete scan is given by $D = NT_t$, where N is the number of projections taken and T_t is the sum of the exposure time and the readout time of the camera. In order to reduce the scan duration, one can use the following approaches:

- reduce N, although there is a lower limit on N to avoid artifacts with conventional algorithms used for the reconstruction of the volumes;
- reduce T_t; or
- reduce N and T_t at the same time by binning pixels (i.e., grouping pixels two by two during acquisition), although this solution results in a lower spatial resolution.

As an example of such optimization, *in situ* experiments of partial remelting in the semisolid state and solidification were performed on Al–Cu at ESRF on the high-energy beamline with binning conditions, using a field of view of 512 × 256 pixels, a spatial resolution of 2.8 μm, and a total scan time of about 15–20 s with 400 projections.[29,61] More recently, *in situ* experiments of partial remelting in the semisolid state and solidification on Al–Cu alloys have been performed under the same conditions but with a wider field of view of 512 × 512 pixels.[62,63] Given these conditions, solidification experiments are limited to low cooling rates (typically a few degrees per minute) and to a solid fraction above the solid coherency fraction in order to avoid grain movements.

Modeling of Semisolid Structures from 3D Data

Analytical Modeling

Three-dimensional data are often used for comparison with analytical modeling of structural evolution of semisolid materials either during isothermal holding or during solidification.

As an example of x-ray tomography on quenched samples, Zabler et al.[57] studied the microstructural evolution in an Al–Ge alloy during isothermal treatment in the semisolid state. They found that the exponent of the power law used to describe the evolution of the mean diameter of solid particles with time is lower than that usually predicted by Lifshitz–Slyozov–Wagner (LSW) theory modified for large solid fractions. *In situ* x-ray tomography experiments on Al–15%Cu samples[62] provided the explanation for this low exponent through a local analysis of particle interactions: It was shown that coalescence and Ostwald ripening occur simultaneously, together with more complex mechanisms involving several particles, for a solid fraction of 0.6.

In situ x-ray tomography has also been performed on an Al–7%Si–10%Cu alloy to study the microstructural evolution during solidification, and the results were compared to analytical modeling of dendrite evolution.[63] Experiments were performed on the high-throughput beamline at ESRF; the time to complete the scan was 20.7 s, and the cooling rate was 3°C/min. This experiment allowed for the *in situ* observation of the continuous growth of the dendrites as shown in Figure 3. Several mechanisms are occurring concurrently, such as dissolution of small secondary arms and filling of the gap between arms. The solid–liquid interface area per unit volume varies as $t^{-1/7}$ (where t is time), indicating a slower kinetics than for models that predict a –1/3 exponent. Experimental values extracted locally on a part of a dendrite where only dissolution of small secondary arms occurs are in good agreement with the analytical model proposed by Chen and Kattamis.[64]

Numerical Modeling

Three-dimensional data on semisolid structures obtained from quenched samples have been used to calculate the permeabilities (i.e., the ability of the solid material to transmit a fluid phase) of such structures. Classically, permeability calculations are made either on 2D real structures[65–68] or from 3D numerical data obtained from a 3D cellular automaton–finite difference model for the growth of a single equiaxed dendrite in a cubic domain.[69] The combination of 3D tomography data as an input in the 3D simulation of the permeability tensor has been investigated on dendritic or equiaxed Al–Cu alloys.[70–72] For equiaxed Al-Cu alloys, 3D tomographs were acquired after rapid quenching of the samples, and 3D simulations were performed to compute the full permeability tensor for

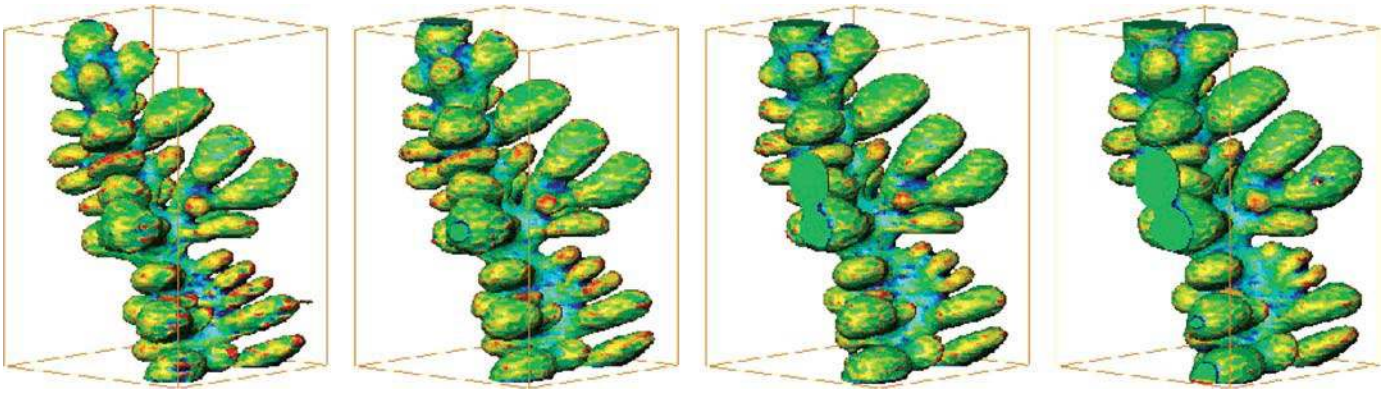

Figure 3. Visualization using fast *in situ* tomography of dendrite evolution during the solidification of an Al–Si–Cu alloy (length of the dendrite ≃ 400 μm). Adapted from Reference 63.

comparison to experimental measurements.[71] Figure 4 presents a comparison of the simulated permeability and the experimental values normalized by the square of the solid–liquid interfacial area. Furthermore, the results were compared to the classical Kozeny–Carman model. The good agreement between experiments and simulations provides confidence in using this approach with 3D data obtained from x-ray tomography as input for permeability simulations.

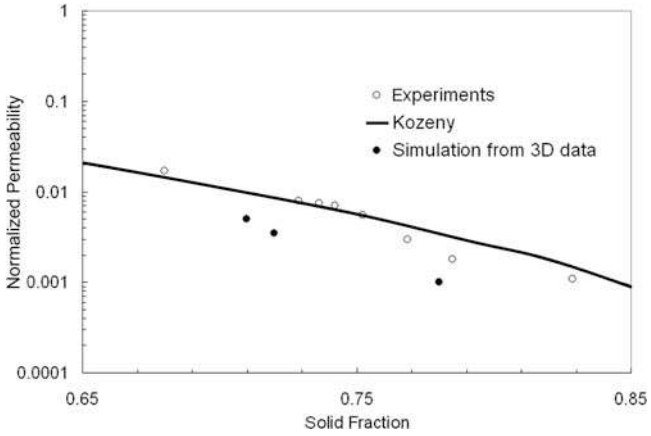

Figure 4. Experimental normalized permeability[71] (white circles) and simulated permeability from 3D data[70] (black circles) as a function of the solid fraction. The classical Kozeny–Carman relationship is also plotted. Adapted from Reference 70.

Propagation of Fatigue Cracks

In structural materials, fatigue cracks initiate from defects such as second-phase particles or pores and therefore have a pronounced three-dimensional shape in their early growth stage. Although this fact was recognized at least 20 years ago,[73] very few models of crack propagation have tried to take it into account, mainly because reliable experimental data were and still are scarce. Indeed, the experimental methods that have been used to characterize the 3D growth of fatigue cracks in optically opaque materials (see Reference 74, for example, for a detailed list) all give indirect information on the crack shape (e.g., compliance or resistivity measurements), and therefore, their applicability to small cracks, typically below 1 mm, is very limited. This is a crucial issue because much of the fatigue life of real components (e.g., aircraft wings, pressure vessels, car motor units) is governed by the growth of small 3D cracks. In addition, in some cases, the influence of the experimental method itself on the propagation can be questioned.

The first attempts to characterize damage with x-ray tomography using medical scanners were limited because of the low resolution available at that time. With the availability of third-generation synchrotron sources in the late 1990s, spatial resolution in the micron range became available, and tomography was used to measure 3D crack openings in an Al alloy under load.[75] Since then, through the use of phase-contrast imaging, which allows for the detection of subvoxel cracks (i.e., cracks with openings that are below the voxel size), three-dimensional images of fatigue cracks have been obtained by researchers in various metallic materials (see Reference 76 for a list). Specifically, diffraction fringes induced by phase contrast underline the crack surface, thereby making the crack detectable in the reconstructed image, as shown in Reference 33. Most such images have been obtained *in situ* and provide either a direct visualization of the complex growth of small fatigue cracks in metals or quantitative information on opening/closure mechanisms.[77–79] All of these experiments have shown crack fronts with irregular shapes (see, for example, details A and B in Figure 5 and compare to the smooth front shown in Figure 6). Although x-ray tomography, in its classical form, cannot visualize grains, in Al alloys, a grain boundary decoration technique (such as Ga infiltration) can be used, making it possible to obtain the 3D shapes of grains surrounding the crack fronts.[30] This technique was applied to demonstrate that crack-front irregularities are correlated with the presence of grain boundaries;[80] crack growth is either favored or impeded in a grain, probably because of favorable/unfavorable local crystallographic orientations.

From the reconstructed 3D images of a growing crack, one can obtain a three-dimensional model of the crack using a finite element code following a slightly modified version of method 2 explained previously. Such models enable calculation of the values of stress intensity factor,

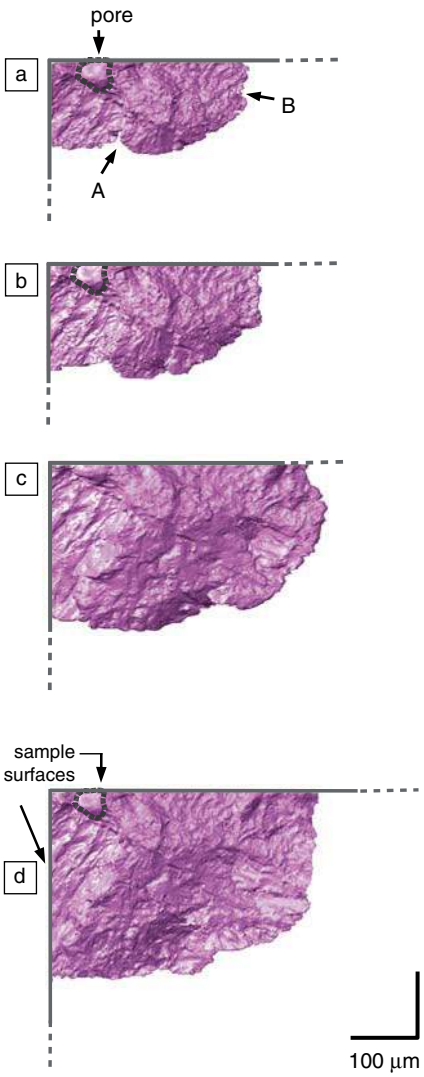

Figure 5. Three-dimensional rendition of a small fatigue crack growing inside a cast Al alloy:[81] The material surrounding the crack has been made transparent so that only one of the crack surfaces appears in the figure. (a) 270,000 cycles, (b) 285,000 cycles, (c) 310,000 cycles, and (d) 320,000 cycles. σ is the applied stress perpendicular to image plane. Letters A and B indicate irregularities on the crack front.

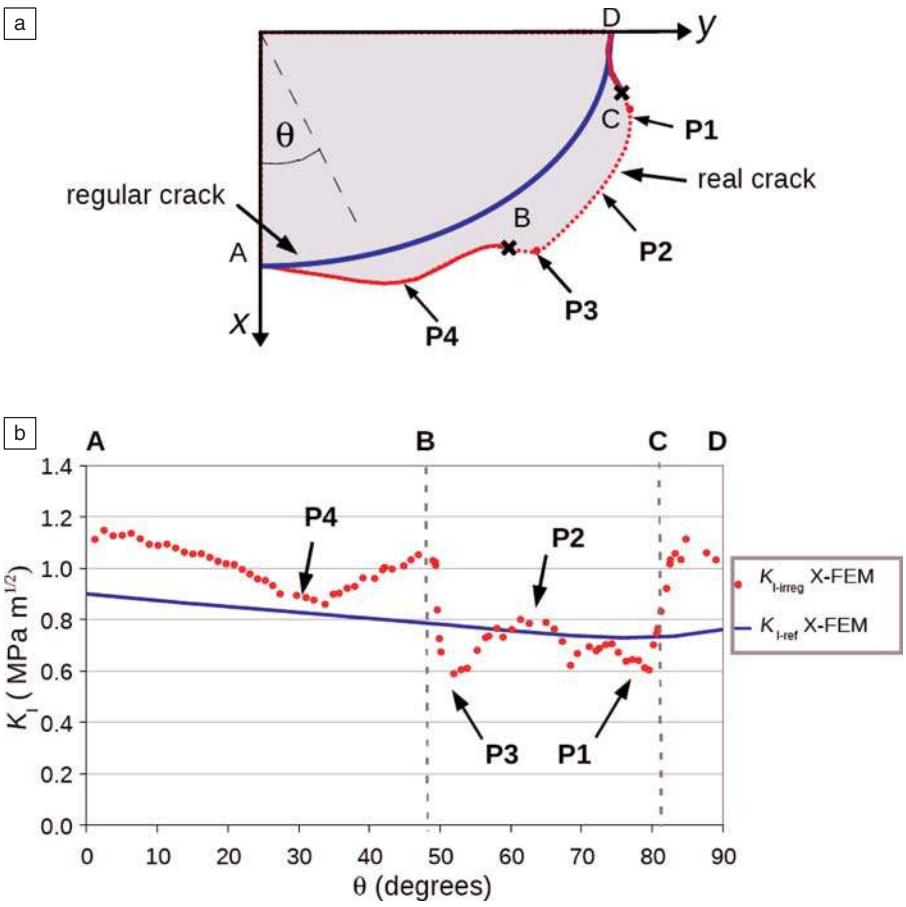

Figure 6. (a) Schematic drawing of the crack shown in Figure 5 after 310,000 fatigue cycles. (b) Values of the mode I stress intensity factor K_I obtained by XFEM on a 3D model of the crack. The solid line represents the variation of K_I for a crack with a smooth front between points A and C.[81]

K, along the crack front and prediction of the propagation of the crack through an appropriate propagation law, which can then be compared to the next experimental crack-front data.[73,81] (The stress field at the tip of a crack is proportional to the value of the stress intensity factor *K*, which is a function of the crack length and of the geometry of the specimen containing the crack.[82]) Modeling of real 3D fatigue cracks with FE is of unprecedented value for the validation of propagation models. However, in practice, compared to calculations on cellular materials or semisolid materials, FE calculations on 3D fatigue cracks face a number of specific challenges:

- "Holes" often appear on the surface that represents the crack in the 3D model as a result of imperfect detection of the crack by automatic image analysis methods.
- Crack fronts often exhibit irregularities that are much smaller than the material grain size, again probably as a result of imperfect detection methods.
- Cracks are generally not planar but exhibit deflections from the plane faces (see, for example, References 30 and 83).

So far, cracks have been considered as continuous planar surfaces with a smooth crack front (i.e., the irregularities mentioned above are ignored) propagating in mode I (that is, the applied load opens the crack perpendicular to its plane[82]). Figure 6 shows the results of calculations of the stress intensity factor obtained with such a crack using the extended finite element method (XFEM); details of the elastic calculation are given elsewhere.[81] It is obvious from this figure that a variation in the crack front shape induces large variations in *K* values at the tip of the crack: a protruding (retreating) front gives a lower (higher) *K* value. If one assumes that protruding parts of the crack front are caused by favorable crystallography, the results of Figure 6 show that this will be balanced by a lower value of the local stress intensity factor. Figure 6 also shows the results obtained for a crack with the same apparent (surface) dimensions but with a smooth crack front. Interestingly, the *K* values at the surfaces for this ideal crack are smaller than those calculated for the real shape. This result, which has been found consistently on similar configurations,[81] might account for the apparent high crack growth rates that are observed for short fatigue cracks.

Three-Dimensional Characterization of the Grain Microstructure in Polycrystalline Materials

Nondestructive characterization of the 3D microstructure of polycrystalline materials in terms of grain shapes and crystallographic orientations constitutes a major experimental challenge in materials science. Currently, two different approaches exist: (1) three-dimensional x-ray diffraction (3DXRD) microscopy, a set of techniques that can be regarded as extensions to the monochromatic beam rotation method (see, e.g., References 9 and 84 for recent reviews and the article in this issue by Juul Jensen et al. for examples of its use), and (2) differential-aperture x-ray microscopy (DAXM),[9,85,86] a wire scanning method based on white-beam Laue diffraction employing a point-focused synchrotron beam. In comparison, 3DXRD allows for *in situ* characterization of millimeter-sized sample volumes (shape, orientation, average strain state of the grains) with a spatial resolution on the order of 5–10 µm, whereas DAXM provides access to the local strain and crystallographic orientation distribution of reduced sample volumes (typically tens of micrometers) with a resolution below 1 µm. Both techniques can be applied to both deformed and undeformed polycrystalline samples. However, none of these diffraction techniques can provide information concerning the local variations of the attenuation coefficient or density. As illustrated earlier, these complementary aspects of a material's microstructure can typically be imaged with the help of x-ray absorption or phase-contrast microtomography.

Here, we present first results[87,88] from a novel tomographic imaging technique that combines the principles of x-ray absorption and x-ray diffraction imaging and that can be regarded as an extension to the above-mentioned 3DXRD methodology. The technique is termed diffraction contrast tomography (DCT),[87,88] underlining its similarity to conventional absorption contrast tomography with which it shares a common experimental setup. With the limitation of being applicable only to undeformed specimens, the grains are imaged using the occasionally occurring diffraction contribution to the x-ray attenuation coefficient each time a grain fulfills the diffraction condition (Figure 7a). A large number of diffraction spots (up to several tens of thousands) are acquired on the 2D high-resolution detector system situated close behind the sample. With an automated image-analysis procedure, these diffraction spots are paired with their corresponding extinction contrast in the direct beam. Based on both spatial and crystallographic constraints, the spot pairs are then sorted into sets belonging to the same grain. Finally, the 3D shapes of each of these grains are reconstructed individually from the limited number of projections available (several tens per grain) using an algebraic reconstruction technique.[89]

After reassembling the grains into a common volume data set, one can visualize the 3D grain microstructure, together with other features (e.g., cracks and inclusions) visible in the absorption image acquired at the same time. As an illustration, Figure 7b shows a 3D rendition of such a reassembled grain volume taken from a 500-µm-diameter sample made from aluminum alloy 1050 (AA1050). The corresponding data set contains about 500 grains and was reconstructed from a total of 7,200 monochromatic-beam (20 keV) projection images with an effective pixel size of 1.4 µm. The required combination of high spatial resolution and accurate monochromatic radiation implies the use of highly intense synchrotron radiation sources in order to limit the total scan acquisition times (typically between 2 and 20 h).

The interest in 3D grain-mapping techniques in general, and in combined imaging and diffraction methods in particular, is related to the unique possibilities they offer. The combination of techniques could enable the study of a variety of physical processes that critically depend on the local crystallographic arrangement and the possible anisotropy it can induce. For instance, one could consider studying grain coarsening processes during heat treatment or analyze the propagation of fatigue or stress corrosion cracks in samples for which the grain structure has been

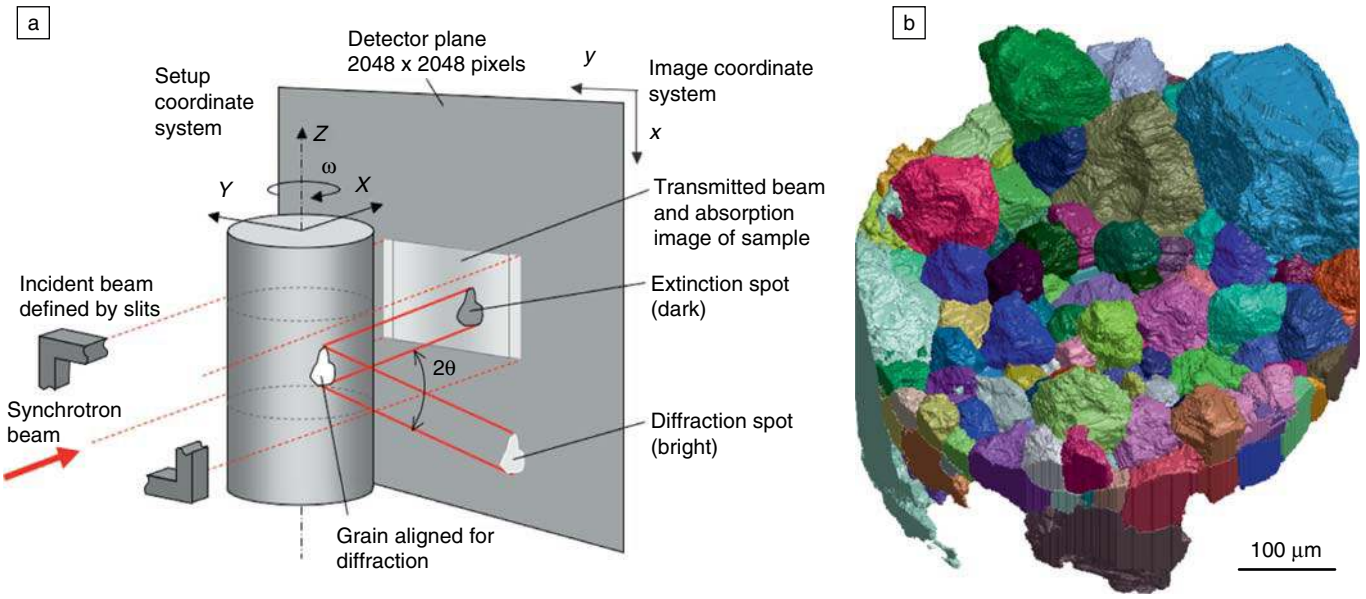

Figure 7. (a) Overview of the acquisition geometry for diffraction-contrast tomography. The footprint of the direct beam (light gray) fills only part of the field of the 2D detector system, which is set close to the sample in order to capture diffraction and absorption information simultaneously. (b) Three-dimensional rendition of the grain structure in a recrystallized AA1050 sample. The grains are colored according to their crystallographic orientation. Reproduced with permission of the International Union of Crystallography.[88]

mapped by DCT in the undeformed state. The comparison of three-dimensional experimental data to numerical simulations can be expected to guide the development of theoretical models, taking into account details of the shape and local crystallographic neighborhood of the grains.

Summary

The availability of third-generation synchrotron x-ray sources has enabled the development of high-resolution x-ray microtomography setups. The designs allow the acquisiton of images of internal features in optically opaque materials with a spatial resolution close to that of optical microscopy. Compared to serial sectioning methods, tomography is non-destructive and therefore permits *in situ* experiments where the evolution of the microstructure of a sample can be followed under various external experimental conditions.

The 3D images obtained contribute primarily to investigations of the physical mechanisms occurring in the bulk of the material (e.g., local buckling of walls in the case of mechanically loaded cellular materials or crack interaction with grain boundaries in fatigued Al alloys) and provide new information on the chronology of the phenomena (e.g., simultaneous coalescence and Ostwald ripening during partial remelting).

Furthermore, 3D meshes can be generated from the reconstructed images by various methods, for use in finite element calculations. Such calculations, based on realistic and representative 3D microstructures, provide quantitative information that can be correlated to the mechanisms observed and that are very useful in testing models.

Finally, novel developments combining 3D imaging with diffraction (diffraction contrast tomography) are emerging. With this new technique, which provides 3D information on the grain shape and crystallographic orientation in polycrystalline samples, the gap between tomography and electron microscopy (with a spatial resolution in the micron range) should be further narrowed. The intersection of the fields should initiate or reinvigorate research in various fields such as damage development or elastic plastic behavior of metals.

Acknowledgments

The authors thank collaborators M. Suery, N. Limodin, E. Boller, M. DiMichiel, D. Bernard, and O. Nielsen and the ANR (French National Agency for Research) for funding through the TOMOSOLIDAL Program. E. Ferrie and A. Gravouil are acknowledged for their help in the *K* calculations using XFEM, and O. Caty is thanked for producing the figures related to the study of the fatigue of cellular materials.

References

1. J.-Y. Buffière, E. Maire, P. Cloetens, G. Lormand, R. Fougeres, *Acta Mater.* **47**, 1613 (1999).
2. C.F. Martin, C. Josserond, L. Salvo, J.J. Blandin, P. Cloetens, E. Boller, *Scripta Mater.* **42**, 375 (2000).
3. J. Radon, *Ber. Verb. Sächs. Akad. Wiss. Leipzig, Math.–Naturwiss. Kl.* **69**, 262 (1917).
4. A.M. Cormack, *J. Appl. Phys.* **34**, 2722 (1963).
5. G.N. Hounsfield, *Br. J. Radiol.* **46**, 1016 (1973).
6. B.P. Flannery, H.W. Deckman, W.G. Roberge, K.L. DAmico, *Science* **237**, 1439 (1987).
7. L. Salvo, P. Cloetens, E. Maire, S. Zabler, J.J. Blandin, J.Y. Buffière, W. Ludwig, E. Boller, D. Bellet, C. Josserond, *Nucl. Instrum. Methods Phys. Res. B* **200**, 273 (2003).
8. E. Maire, J.Y. Buffière, L. Salvo, J.J. Blandin, W. Ludwig, J.M. Letang, *Adv. Eng. Mater.* **3**, 539 (2001).
9. C.G. Schroer, P. Cloetens, M. Rivers, A. Snigirev, A. Takeuchi, W.B. Yun, *MRS Bull.* **29**, 157 (2004).
10. J. Banhart, ed., *Advanced Tomographic Methods in Materials Research and Engineering*, (Oxford University Press, Oxford, UK, 2008).
11. http://www.phoenix-xray.com/en/index.php, http://www.skyscan.be/home.htm, http://www.xtekxray.com/, http://www.xradia.com.
12. A. Sakellariou, T.J. Sawkinsa, T.J. Sendena, A. Limaye, *Physica A* **339**, 152 (2004).
13. B.C. Masschaele, V. Cnudde, M. Dierick, P. Jacobs, L. Van Hoorebeke, J. Vlassenbroeck, *Nucl. Instrum. Methods Phys. Res., Sect. A* **580**, 266 (2007).
14. H. Toda, K. Uesugi, A. Takeuchi, K. Minami, M. Kobayashi, T. Kobayashi, *Appl. Phys. Lett.* **89**, 143112 (2006).
15. R. Mokso, P. Cloetens, E. Maire, W. Ludwig, J.Y. Buffière, *Appl. Phys. Lett.* **90**, 144104 (2007).
16. D.J. Rowenhorst, A. Gupta, C.R. Feng, G. Spanos, *Scripta Mater.* **55**, 11 (2006).
17. D.M. Saylor, J. Fridy, B.S. El-Dasher, K.Y. Young, A.D. Rollett, *Metall. Trans. A* **35**, 1969 (2004).
18. A.D. Rollett, S.B. Lee, R. Campman, G.S. Rohrer *Annu. Rev. Mater. Res.* **37**, 627 (2007).
19. M.D. Uchic, M.A. Groeber, D.M. Dimiduk, J.P. Simmons, *Scripta Mater.* **55**, 23 (2006).
20. R. Parisot, S. Forest, A. Pineau, F. Nguyen, X. Demonet, J.-M. Mataigne, *Metall. Mater. Trans. A* **35**, 797 (2004).
21. A.C. Lewis, J.F. Bingert, D.J. Rowenhorst, A. Gupta, A.B. Geltmacher, G. Spanos, *Mater. Sci. Eng. A* **418**, 11 (2006).
22. D. Kammer, R. Mendoza, P.W. Voorhees, *Scripta Mater.* **55**, 17 (2006).
23. J.H. Kinney, M.C. Nichols, *Annu. Rev. Mater. Sci.* **22**, 121 (1992).
24. S.F. Nielsen, H.F. Poulsen, F. Beckman, C. Thorning, J.A. Wert, *Acta Mater.* **59**, 437 (2003).
25. L. Qian, H. Toda, K. Uesugi, T. Kobayashi, T. Ohgaki, M. Kobayashi, *Appl. Phys. Lett.* **87**, 241907 (2005).
26. F. De Carlo, X.H. Xiao, B. Tieman, *Proc. SPIE: Int. Soc. Opt. Eng.* **6318**, K3180 (2006).
27. B.J. Connolly, D.A. Homer, S.J. Fox, A.J. Davenport, C. Padovani, S. Zhou, A. Turnbull, M. Preuss, N.P. Stevens, T.J. Marrow, J.Y. Buffière, E. Boller, A. Groso, M. Stampanoni, *Mater. Sci. Technol.* **22**, 1076 (2006).
28. F. Beckmann, R. Grupp, A. Haibel, M. Huppmann, M. Nöthe, A. Pyzalla, W. Reimers, A. Schreyer, R. Zettler, *Adv. Eng. Mater.* **9**, 939 (2007).
29. O. Ludwig, M. DiMichiel, L. Salvo, M. Suéry, P. Falus, *Metall. Trans. A* **36**, 1515 (2005)
30. W. Ludwig, J.-Y. Buffière, S. Savelli, P. Cloetens, *Acta Mater.* **51**, 585 (2003).
31. A.C. Kak, M. Slaney, *Principles of Computerized Tomographic Imaging* (Society for Industrial and Applied Mathematics, Philadelphia, PA, 2001).
32. J.C. Labiche, O. Mathon, S. Pascarelli, M.A. Newton, G. Guilera Ferre, C. Curfs, G. Vaughan, A. Homs, D. Fernandez Carreiras, *Rev. Sci. Instrum.* **78**, 091301 (2007).
33. P. Cloetens, M. Pateyron-Salome, J.-Y. Buffière, G. Peix, J. Baruchel, F. Peyrin, M. Sclenker, *J. Appl. Phys.* **81**, 5878 (1997).
34. L. Gibson, M. Ashby, *Cellular Solids, Structure and Properties* (Pergamon Press, Oxford, UK, 1988).
35. A.P. Roberts, E.J. Garboczi, *Acta Mater.* **49**, 189 (2001).
36. D. Ulrich, B. Van Rietbergen, H. Weinans, P. Ruegsegger, *J. Biomech.* **31**, 1187 (1998).
37. E. Maire, A. Fazekas, L. Salvo, R. Dendievel, S. Youssef, P. Cloetens, J.M. Letang, *Compos. Sci. Technol.* **63**, 2431 (2003).
38. A. Borbély, P. Kenesei, H. Biermann, *Acta Mater.* **54**, 2735 (2006).
39. R. Jancek, A. Kottar, B. Kriszt, H.P. Degischer, in *Proc. Symp. Cell. Met. Polym.* (Trans Tech Publications, 2005), pp. 107.
40. S. Youssef, E. Maire, R. Gaertner, *Acta Mater.* **53**, 719 (2005).
41. K. Madi, S. Forest, M. Boussuge, S. Gaillièguе, E. Lataste, J.-Y. Buffière, D. Bernard, D. Jeulin, *Comput. Mater. Sci.* **39**, 224 (2007).
42. J.A. Elliott, A.H. Windle, J.R. Hobdel, G. Eeckhaut, R.J. Oldman, W. Ludwig, E. Boller, P. Cloetens, J. Baruchel, *J. Mater. Sci.* **37**, 1547 (2002).
43. P.R. Onck, R. van Merkerk, J.T.M. De Hosson, I. Schmidt, *Adv. Eng. Mater.* **6**, 6 (2004).
44. E. Maire, N. Gimenez, V. Sauvant-Moynot, H. Sauterau, *Philos. Trans.* **364**, 69 (2006).
45. Z. Liang, M.A. Ioannidis, I. Chatzis, *J. Colloid Interface Sci.* **221**, 13, (2000).
46. J.E. Spowart, *Scripta Mater.* **55**, 5 (2006).
47. Y. Ito, M.C. Flemings, J.A. Cornie, in *Nature and Properties of Semi-Solid Materials*, J.A. Sekhar, J. Dantzig, eds. (TMS, Warrendale, PA, 1992), pp. 3–17.
48. B. Niroumand, K. Xia, *Mater. Sci. Eng.* **A283**, 70 (2000).
49. J. Alkemper, P.W. Voorhees, *Acta Mater.* **49**, 897 (2001).
50. J. Alkemper, R. Mendoza, P.W. Voorhees, *Adv. Eng. Mater.* **4**, 694 (2002).
51. R. Mendoza, J. Alkemper, P.W. Voorhees, *Metall. Trans. A* **34**, 481 (2003).
52. D. Kammer, P.W. Voorhees, *Acta Mater.* **54** (6), 1549 (2006).

53. D.J. Rowenhorst, J.P. Kuang, K. Thornton, P.W. Voorhees, *Acta Mater.* **54**, 2027 (2006).
54. S. Verrier, M. Braccini, C. Josserond, L. Salvo, M. Suéry, P. Cloetens, W. Ludwig, in *Proc. 6th Intl. Conf. on Semi-Solid Processing of Alloys and Composites*, G.L. Chiarmetta, M. Rosso, Eds. (Edimet Spa, Brescia, 2000), pp. 771.
55. S. Zabler, A. Rueda, A. Rack, H. Riesemeier, P. Zaslansky, I. Manke, F. Garcia-Moreno, J. Banhart, *Acta Mater.* **55** (15), 5045 (2007).
56. L. Salvo, M. Suéry, C. Josserond, P. Cloetens, O. Nielsen, *Proc. 7th Int. Conf. on Advanced Semisolid Processing of Alloys and Composites*, Y. Tsutsui, M. Kiuchi, K. Ichikawa, Eds. (2002), pp. 403.
57. S. Zabler, A. Haibel, A. Lohmüller, J. Banhard, A. Rueda, A. Rack, H. Riesemeier, J. Goebbels, T. Wolk, G. Weidemann, 9th European Conference on NDT, Berlin, Germany, September 2006, We.1.5.2, pp. 1–7.
58. O. Pompe, M. Rettenmayr, *J. Cryst. Growth* **192**, 300 (1998).
59. R. Mokso, PhD dissertation, Université Joseph Fourier, Grenoble, France 2006 .
60. M. Di Michiel, J.M. Merino, D. Fernandez-Carreiras, T. Buslaps, V. Honkimaki, P. Falus, T. Martins, O. Svensson, *Rev. Sci. Instrum.* **76**, 043702, (2005).
61. O. Ludwig, M. DiMichiel, P. Falus, L. Salvo, M. Suéry, presented at the 8th S2P Conf. on Semisolid Processing of Alloys and Composites, Limassol, Cyprus, 21–23 September 2004 (NADCA, USA).
62. N. Limodin, L. Salvo, M. Suery, M. DiMichiel, *Acta Mater.* **55**, 3177 (2007).
63. N. Limodin, E. Boller, L. Salvo, M. Suéry, M. DiMichiel, *Proc. 5th Decennial Int. Conf. on Solidification Processing*, H. Jones, Ed. (University of Sheffield, UK, 23–25 June 2007), p. 316.
64. M. Chen, T.Z. Kattamis, *Mater. Sci. Eng. A* **247**, 239 (1998).
65. S. Ganesan, C.L. Chan, D.R. Poirier, *Mater. Sci. Eng.* **151**, 97 (1992).
66. J.F. McCarthy, *Acta Mater.* **42**, 1573 (1994).
67. M.S. Bhat, D.R. Poirier, J.C. Heinrich, *Metall. Mater. Trans. B* **26**, 1049 (1995).
68. B. Goyeau, T. Benihaddadene, D. Gobin, M. Quintard, in *Modeling of Casting, Welding and Advanced Solidification Processes VIII*, B.G. Thomas, C. Beckermann, eds. (TMS, Warrendale, PA, 1998), p. 353.
69. S.G.R. Brown, J.A. Spittle, D.J. Jarvis, R. Walden-Bevan, *Acta Mater.* **50**, 1559 (2002).
70. D. Bernard, O. Nielsen, L. Salvo, P. Cloetens, *Mater. Sci. Eng. A* **392**, 112 (2005).
71. Ø. Nielsen, L. Arnberg, A. Mo, H. Thevik, *Metall. Mater. Trans. A* **30**, 2455 (1999).
72. D. Fuloria, P.D. Lee, D. Bernard, *Proc. 5th Decennial Int. Conf. on Solidification Processing*, H. Jones, Ed. (University of Sheffield, UK, 23–25 June 2007), p. 685.
73. K.J. Miller Fat. Frac. Eng. Mat. Struct. 10 75 (1987).
74. E. Ferrie, J.-Y. Buffière, W. Ludwig, A. Gravouil, L. Edwards, *Acta Mater.* **54**, 1111 (2006).
75. A. Guvenilir, T.M. Breunig, J.H. Kinney, S.R. Stock, *Acta Mater.* **45**, 1977 (1997).
76. J.-Y. Buffière, E. Ferrie, H. Proudhon, W. Ludwig, *Mater. Sci. Technol.* **22**, 1019 (2006).
77. H. Toda, I. Sinclair, J.-Y. Buffière, E. Maire, K.H. Khor, P. Gregson, T. Kobayashi, *Acta Mater.* **52**, 1305 (2004).
78. K.I. Ignatiev, W.K. Lee, K. Fezzaa, S.R. Stock, *Philos. Mag.* **85**, 3273 (2005).
79. P.J. Withers, J. Bennett, Y.-C. Hung, M. Preuss, *Mater. Sci. Technol.* **22**, 1052 (2006).
80. E. Ferrie, J.-Y. Buffière, W. Ludwig, *Int. J. Fatigue* **27**, 1215 (2005).
81. E. Ferrie, PhD thesis, Institut National des Sciences Appliquées de Lyon (INSA Lyon), Lyon, France, 2006; http://csidoc.insa-lyon.fr/these/pont.php?id=ferrie.
82. J.F. Knott, *Fundamentals of Fracture Mechanics* (Butterworths, London 1981).
83. K.H. Khor, J.-Y. Buffière, W. Ludwig, I. Sinclair, *Scripta Mater.* **55**, 47 (2006).
84. H.F. Poulsen, *Three-Dimensional X-ray Diffraction Microscopy. Mapping Polycrystals and Their Dynamics* (Springer Tracts in Modern Physics, Vol. 205, Springer, Berlin, 2004).
85. B.C. Larson, W. Yang, G.E. Ice, J.D. Budai, J.Z. Tischler, *Nature* **415**, 887 (2002).
86. G.E. Ice, B.C. Larson, W. Yang, J.D. Budai, J.Z. Tischler, J.W.L. Pang, R.I. Barabash, W. Liu, *J. Synchrotron Radiat.* **12**, 155 (2005).
87. W. Ludwig, S. Schmidt, E.M. Lauridsen, H.F. Poulsen, *J. Appl. Crystallogr.*, 41 302 (2008).
88. G. Johnson, A. King, M. Gonzalves-Hoennicke, W. Ludwig, *J. Appl. Crystallogr.*, 41, 310 (2008).
89. R. Gordon, R. Bender, G.T. Herman, *J. Theor. Biol.* **29**, 471 (1970).
90. O. Caty, E. Maire, R. Bouchet. *Adv. Eng. Mater.* **10,** 179 (2008).